# Alma Mater Studiorum Università di Bologna
# Archivio istituzionale della ricerca

Stiffness prediction and deformation analysis of Cobalt-Chromium lattice structures: From periodic to functionally graded structures produced by additive manufacturing

29 June 2024

# Stiffness prediction and deformation analysis of Cobalt-Chromium lattice structures: from periodic to functionally graded structures produced by additive manufacturing

Erica Liverani [(a,*)], Alessandro Fortunato [(b)]

[(a)] Interdepartmental Center for Industrial Research - Advanced Applications in Mechanical Engineering and Materials Technology (CIRI – MAM), Alma Mater Studiorum - University of Bologna, Bologna (Italy)
[(b)] Department of Industrial Engineering (DIN), Alma Mater Studiorum - University of Bologna, Bologna (Italy)
[(*)] Corresponding author. E-mail address: erica.liverani2@unibo.it

## Abstract

Lattice structures are candidates for innovative design of orthopedic implants and other highly functional products. In particular, functionally graded structures can be employed to achieve the required strength and stiffness for optimal stress-strain distribution. Prediction of the real behavior of these structures is essential for effective design. In the present work, stiffness prediction and deformation analysis of Cobalt-Chromium lattice structures manufactured using laser-based Powder Bed Fusion additive manufacturing were carried out. The study was developed in two steps: compressive tests and Digital Image Correlation were performed on periodic structures, with the results used to predict the stiffness of two types of functionally graded structures. The proposed method was validated experimentally, with the predicted stiffness of structures designed with the proposed elementary units within 6.1 % for all tested cases. An array of stiffness data was then defined to allow free design of graded structures foreseeing specific compressive properties. The mechanical properties and deformation behavior of the structures were also investigated, with the local strain distribution mapped and compared to global deformation values.

## Keywords

Laser-Based Powder Bed Fusion; Functionally Graded Structures; Stiffness Prediction

## 1. Introduction

Additive manufacturing (AM) technology and, in particular, Laser-based Powder Bed Fusion (LPBF), enable the fabrication of structures with geometry that is unachievable with traditional manufacturing methods. Not only can LPBF produce components with complex geometry [1], but it can be employed to fill simple volumes with arbitrary complex lattice structures [2, 3]. Before LPBF, many other methods to make 3D porous lattice structures were used, all of which involved metal foams produced mainly with powder metallurgy, metal deposition, metallic melt foaming,

investment casting and infiltration casting [4]. These processes allowed the production of stochastic porous structures with a random distribution of solid matter and so could not guarantee the same geometric and mechanical properties as structures designed to achieve a specific purpose.

The main advantage of LPBF processes is essentially the possibility of producing geometrically ordered lattice components with three-dimensional open-celled structures composed of one or more repeating unit cells [5, 6]. These units are defined by their dimensions, form and porosity. In particular, the cells are conventionally categorized into two distinct groups: strut-based or triply periodic minimal surfaces (TPMS). TPMS structures are generated using mathematical formulae that define the zero iso-surface boundary between solid and void sections of the structure [7]. Strut-based units are simple design units described by their constituent strut elements and connection nodes. Both structures are very easy to design and produce with LPBF. Though a lot of experimental and theoretical work has been performed to understand and predict lattice structure behavior [8,9], their potential uses are numerous and more work is required.

In order to understand the importance of lattice structures in the fabrication of highly functional products, Bathe *et al.* [10] proposed an overall picture of their applications. For example, the development of designed porous materials allows mass reduction of mechanical parts for either strain or vibration isolation [11]. Beyond structural mechanics, it is important to cite thermo-mechanical applications that exploit the large surface area of lattices to aid heat transfer [12,13]. A well-designed lattice structure can provide a range of heat transfer properties including heat exchange, heat shielding or insulation.

Lattice structures have also been successfully applied to the fabrication of biomedical devices to enhance osseointegration and/or to reduce stress shielding phenomena [14-17].

Functionally Graded (FG) lattice structures [7,18,19], where the size and shape of unit cells are varied to achieve local part functionality (e.g. stiffness to prevent stress shielding on bone, shape for increasing cell viability, etc.), can provide remarkable advantages to biomedical products.

Correct design of FG structures before printing provides great benefits to patients that are subject to total or partial prostheses replacements. However, one of the main challenges in the fabrication of FG structures, for all the cited applications, deals with the prediction and the reliability of the results of the entire process. The fabrication of lattice structures demands a high degree of architectural control in order to produce the desired mechanical properties.

Despite some studies have shown that, in limited conditions, it is possible to obtain reliable results [20], simulation outcomes often do not agree with real mechanical properties due to the great number of variables involved in LPBF processes and difficultly in their prediction [21-24]. Among the different variables, the most important include: (i) the quantity of un-melted powder sintered to the surface of lattice beam struts; (ii) the real dimensions of struts within the lattice and (iii) anisotropy, residual stress and deformation. Choy *et al* [25] and Yang *et al* [26] studied the manufacturability and the corresponding mechanical response of FG lattice structures respectively produced by EBM and LPBF processes. Both studies have highlighted the not-negligible effects of process on geometrical accuracy and the relation between geometric variations and lattice compressive behavior. Yang *et al* [26], in particular, underlined that the experimental mechanical properties are higher than FE prediction due to geometric deviations between designed and real samples. In order to overcome these critical issues, Sudarmaji *et al* [27] proposed mathematical relations correlating polycaprolactone scaffolds structure and porosity to their corresponding compressive stiffness.

In this paper the authors focused on defining an experimental method for estimating the mechanical behavior of lattice structures produced by additive manufacturing. The approach aims at predicting the stiffness of periodic and graded lattice structures based on data obtained with simple structures and extended to components of different sizes. The local stiffness of three different periodic structures previously design by the authors [14] was measured during compressive tests using Digital Imaging Correlation (DIC), with the stiffness of each single unit subsequently calculated. From these data, the stiffness of two different FG structures was predicted and confirmed with the same experimental method. Finally, an array of stiffness values was calculated analytically by varying the macroscopic dimensions of the structures in terms of the number of layers and units per layer, with the accuracy of the data map assessed experimentally by printing two structures with different geometry. The deformation behavior and failure mode of the proposed units were also investigated, with the local strain distribution studied and compared to global deformation values.

The main field of application addressed within this paper relates to the manufacture of custom endoprostheses. Up to 50% of failures relating to this type of implant are a consequence of inadequate bone-to-implant osseointegration, for which the introduction of a lattice interface is a valid approach to overcoming these issues [28].

## 2. Material and methods

### 2.1 Design and manufacturing

The single unit employed within the study consisted of a 1.5 mm cubic element perforated with holes of different diameters to obtain a range of structural densities (the ratio of equivalent full density to lattice component) of between 37 % and 67 %. These units can be reproduced in a three-dimensional array or even mixed together. In all cases, structural continuity of the lattice and interconnection of the internal cavities was ensured.

Both the periodic and FG strut samples were designed using the aforementioned units in three different sizes. The nominal diameters of holes were 0.50 mm, 0.75 mm, and 1 mm, shown from left to right in Figure 1. Periodic samples were designed by repeating the same unit to obtain structures with 10 overlapping layers, each made up of 8x8 units. The naming convention used for these samples was based on the nominal diameter of the holes preceded by the prefix P (periodic) (i.e. P0.5, P0.75, P1 for periodic structures with 0.5 mm, 0.75 mm and 1 mm holes, respectively).
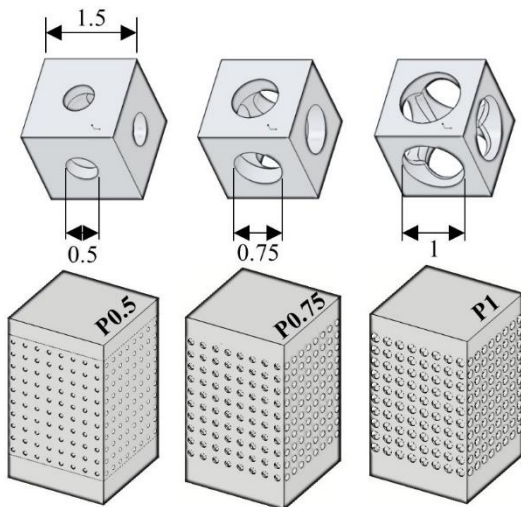


Figure 1: Samples: single units and periodic lattice structures used for tests.

The FG structures were designed using two different strategies. In the first, layers with increasing structural density were overlaid from top to bottom (Figure 2a), while in the second, high-density layers were positioned at the center of samples with decreasing density towards both the bottom and the top (Figure 2b). These samples were named FG1 and FG2, respectively.
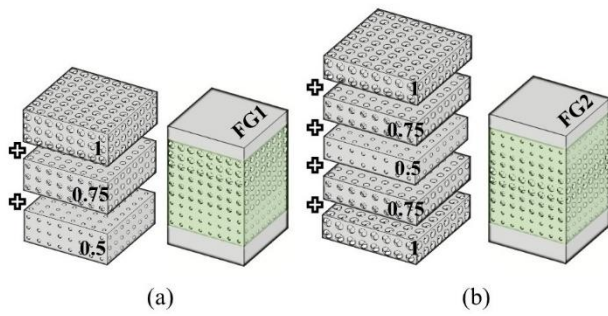
Figure 2: Samples: Functionally Graded structures used for tests (a) FG1, (b) FG2.

Finally, two different sized structures (Figure 3) were designed with 0.75 mm units and manufactured to verify the predicted stiffness array. Figure 3a shows a 10-layer sample denominated T0.75 (T = tall) with 5x5 units per layer, while Figure 3b shows a 4-layer sample denominated S0.75 (S = short) with 8x8 units per layer.
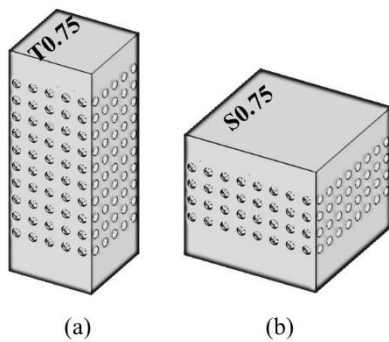


Figure 3: Samples: Periodic structures used for verification of the proposed stiffness model. Samples (a) T0.75 and (b) S0.75.

Four samples of each type were manufactured via LPBF in a biocompatible cobalt-based alloy (CoCrMo). The powder, supplied by Carpenter Technology under the product name Cobalt Chrome F75, meets the ASTM F75 standard for surgical implants. The reported powder composition was 27-30% chromium, 5-7% molybdenum, 0.75% iron, less than 1% manganese and silicon, less than 0.5% nickel, less than 0.1% other elements and the balance being cobalt. The powder was obtained by the manufacturer with a standard gas atomization procedure whereby feedstock was initially melted in a vacuum, after which the chamber was backfilled with nitrogen gas to force the molten alloy through a nozzle. A high-velocity gas jet then impinged on the melt flow to break it into small spherical droplets and, upon solidification and cooling, a sieving procedure was employed to obtain particles in the standard range of 15-45 μm.

The additive manufacturing machine used for production of the samples was a SISMA MYSINT100 RM equipped with a fiber laser with power output of up to 175 W and a focused spot size of 55 μm. The process was carried out in a nitrogen environment with a residual oxygen content of 0.2 vol.%.

No attempt was made to explore the effects of varying process parameters beyond those described in a previous work [15], summarized in Table 1. A 3x3 mm chessboard scanning strategy was used for hatching. The laser path for two representative layers is shown in Figure 4. The built direction was parallel to the sample height in all cases.

Table 1: Process parameters for CoCrMo lattice structure production.

| Laser power [W] | Scan speed [mm/s] | Layer thickness [μm] | Hatch spacing [μm] | Scanning strategy |
|---|---|---|---|---|
| 130 | 1200 | 20 | 70 | 3x3 mm chessboard |
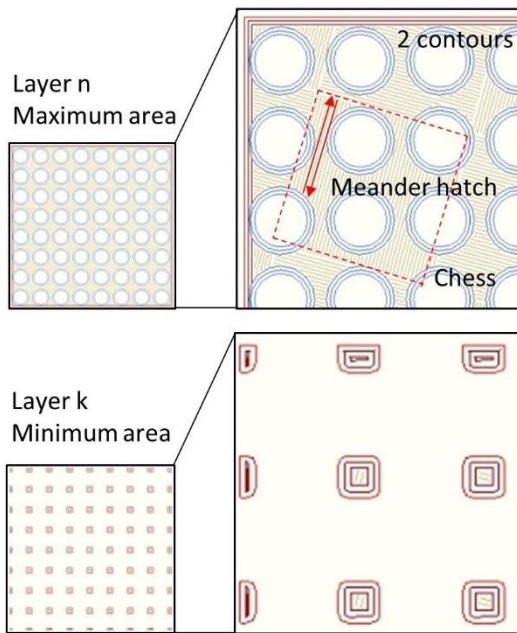


Figure 4: Scanning strategy: laser path used for LPBF production of lattice structures.

## 2.2 Compressive tests and DIC analysis

The upper and lower surfaces of samples were milled to remove all traces of supports and ensure that they were parallel for correct distribution of the load during compressive tests. Samples were subsequently prepared for DIC (Digital Image Correlation) analysis to obtain a random speckle pattern on the surface under analysis. The artificial pattern was produced by spraying black paint dots on a white background.

Uniaxial compressive tests were performed on three samples of each type at room temperature on an Italsigma servo-hydraulic load press with a 100 kN load cell in line with ISO 13314 for porous materials. Each test was performed at a strain rate of approximately 0.0005 s$^{-1}$. Test data were acquired with two parallel, independent acquisition systems. The press control software acquired load and displacement data at 10 Hz, with displacement data also acquired with an extensometer. In parallel, a LabVIEW program was used to stored camera frames that were captured manually at constant load steps (5 kN for P0.5 samples, 3 kN for P0.75 samples and 1 kN for all other geometries) together with a data file containing the corresponding load for each frame. The camera was a 6.4 MPx Basler acA3088-57μm positioned on an adjustable pedestal. Two led strips were mounted on a support behind the camera for correct illumination of the setup.

The resulting global mechanical behavior was described with a stress-strain curve to examine the main properties of the tested lattice structures. A more detailed description of the flow stress curve was considered based on the Johnson & Cook (J&C) constitutive model, neglecting the effects of temperature and strain rate.

The relationship given by the J&C model is reported in Equation 3, where $\sigma_f$ is the plastic stress [MPa], $\varepsilon$ is the plastic strain [μm/μm] and A [MPa], B [MPa] and n are material-specific coefficients determined through analysis of the stress-strain curve.

Equation 1:

$$\sigma_f = A + B\varepsilon^n$$

Coefficients A and B were derived using a standard methodology for curve fitting within the MatLab software (version R2019b) [29].

DIC data were processed with GOM Correlate software to obtain the local displacement and strain of each pixel identified within a user-defined area of each captured frame. Data analysis and processing were carried out for the periodic components (Figure 1) in four successive steps: (i) derivation of the overall stiffness of component from DIC data ($k_{TOT}$), (ii) measurement of the stiffness of each layer from DIC data ($k_L$), (iii) indirect calculation of the stiffness of the single unit and (iv) comparison of local strain concentrations with the nominal compression strain. The single unit stiffness ($k_U$) was calculated as the ratio of layer stiffness to the number of units per layer.

From these results, stiffness prediction was performed for the FG1 and FG2 samples using the following theoretical equations (Equation 1,2), derived from series and parallel spring theory:

Equation 2:

$$k_{FG,nth\ layer} = NU_{Pn} \cdot k_{U,Pn} ; \quad \frac{1}{k_{FG,tot}} = \sum \frac{NL_{Pn}}{NU_{Pn} \cdot k_{U,Pn}}$$

Equation 3:

$$\frac{1}{k_{FG,tot}} = \frac{NL_{P1}}{k_{U,P1} \cdot NU_{P1}} + \frac{NL_{P0.75}}{k_{U,P0.75} \cdot NU_{P0.75}} + \frac{NL_{P0.5}}{k_{U,P0.5} \cdot NU_{P0.5}} = \begin{cases} \dfrac{3}{k_{U,P1} \cdot 64} + \dfrac{3}{k_{U,P0.75} \cdot 64} + \dfrac{3}{k_{U,P0.5} \cdot 64} & (FG1) \\[2ex] \dfrac{2}{k_{U,P1} \cdot 64} + \dfrac{4}{k_{U,P0.75} \cdot 64} + \dfrac{4}{k_{U,P0.5} \cdot 64} & (FG2) \end{cases}$$

where:

$NL_{P1}$, $NL_{P0.75}$, $NL_{P0.5}$ = number of layers designed with P1, P0.75 and P0.5 units, respectively

$NU_{P1}$, $NU_{P0.75}$, $NU_{P0.5}$ = number of P1, P0.75 and P0.5 units placed in each assigned layer, respectively

$k_{U,P1}$, $k_{U,P0.75}$, $k_{U,P0.5}$ = Single unit (P1, P0.75 and P0.5) stiffness

$k_{FG}$ = stiffness of functionally graded sample

Subsequently, the obtained theoretical values were compared with measurements of the experimental stiffness of the overall FG structures obtained with DIC. Based on these outcomes, a stiffness array was then defined for structures with various numbers of units for each layer, from 2x2 to 10x10, and various numbers of layers, from 1 to 15. Validation of this matrix was performed by testing the samples shown in Figure 3.

### 2.3 Defects, microstructural analysis and geometrical accuracy

Evaluation and analysis of microstructural and geometric defects was carried out with a Scanning Electron Microscope (SEM, Philips XL20) and Optical Microscope (OM, Nikon Optiphot-100).

For microstructural analysis, a cross-section parallel to the lattice build direction was obtained on one sample of each geometry. Samples were prepared using conventional procedures comprising mechanical grinding (80–2000 grit papers) and polishing with alumina in suspension down to a particle size of 0.6 μm.

Optical microscopy was performed both before and after electrochemical etching at 4 V for 20 s in a solution of hydrochloric acid and ferric chloride dissolved in distilled water (10 mL HCl, 20 g FeCl3, 200 mL H2O).

The struts continuity and holes interconnection were evaluated by the same optical microscope. The lattices density was calculated using Archimedes' principle with the mass of the sample

measured by a weighing machine (Radwag balance, Type PS600 R2) in air and distilled water, respectively. The volume of each sample was derived by the ratio of the mass of the sample in air to its density. The geometric accuracy of the sample was subsequently derived as a ratio of the measured volume to the nominal volume, returned by CAD design.

## 3. Results

### 3.1 DIC analysis during compressive tests

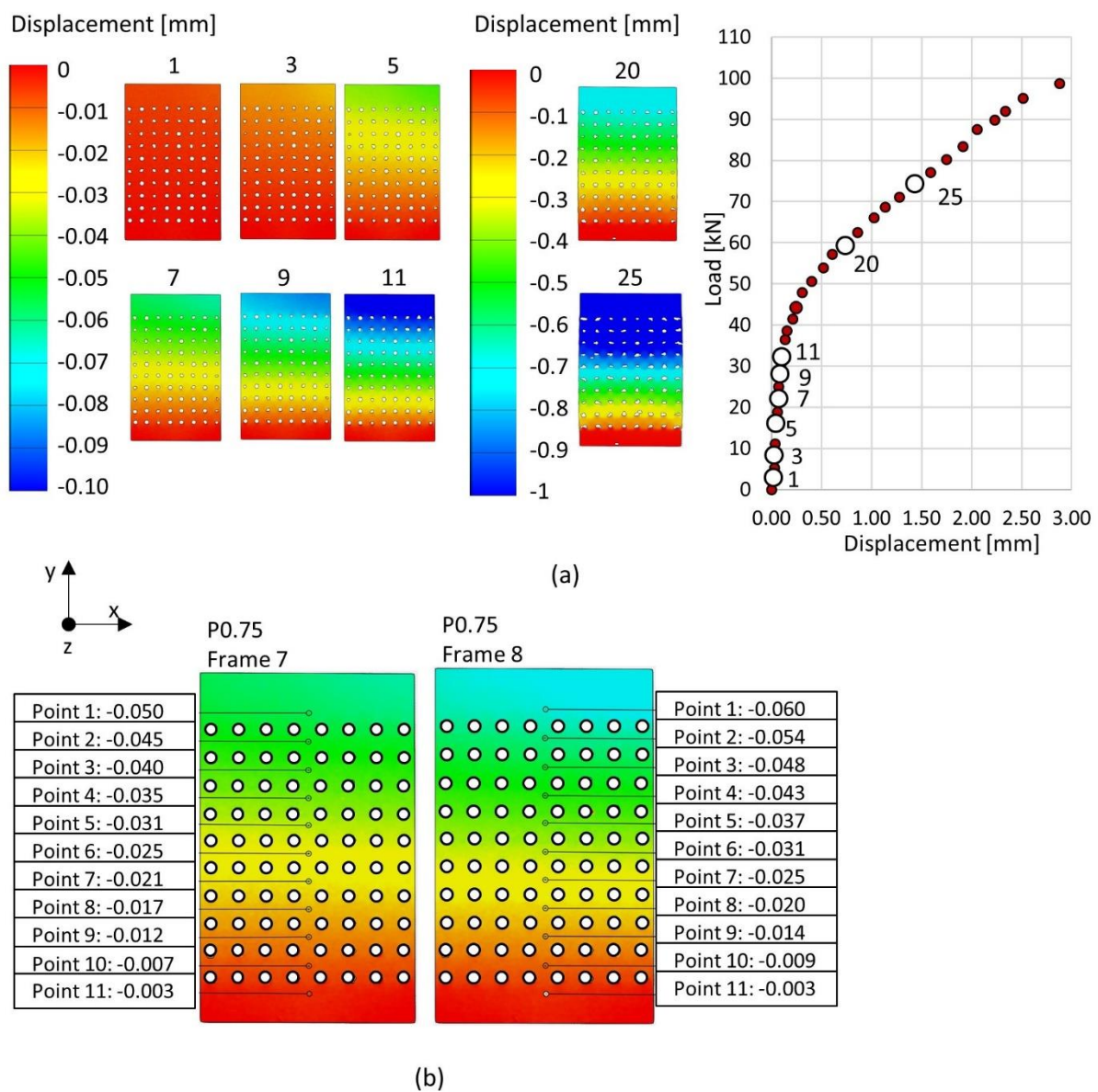#### 3.1.1 Stiffness measurement of periodic structures



(a)



(b)

Figure 5: DIC analysis: (a) displacement maps of a P0.75 periodic structure and corresponding load-displacement curve. (b) Detailed measurement of layer displacements.

The displacement maps obtained from DIC analysis of each frame were initially used to measure the total displacement and detect misalignments for all structures. An example of such a map is reported on the left-hand side of Figure 5a. Moreover, examination of the same values during elastic deformation allowed calculation of the overall stiffness of each structure. The total stiffness represented a value with which the measured data for each layer could be compared. Figure 5 shows an example of the procedure used for measurement of layer stiffness relating to the periodic P0.75 sample.

The elastic deformation section was then identified for each load-displacement curve. As an example, this section is between frames 1 and 11 in Figure 5a, highlighted with white dots. All frames were accurately analyzed, with the displacement of each layer measured, as show in Figure 5b for two subsequent images. Each probe was located at the intersection between a central y-z section and a z-x plane passing between the layers. Therefore, the labels reported in Figure 5b indicate the displacement (mm) of the probe with respect to the unloaded reference position of the same point (frame 0).

Data processing of all frames led to compilation of a table similar to that shown in Table 2 for the P0.75 structure referenced above. In order to simplify interpretation, Table 2 is an extract of the overall layout showing only data relating to three frames (6-7-8) and three probes (4-5-6).

Figure 6 presents the calculated values graphically for each periodic sample (P0.5, P0.75 and P1), together with the respective standard deviations. Once the stiffness value of each plane was known, the single unit stiffness was calculated as described in Section 2.2. Table 3 summarizes the resulting mean values.

Table 2: Displacement data processing for stiffness calculation.

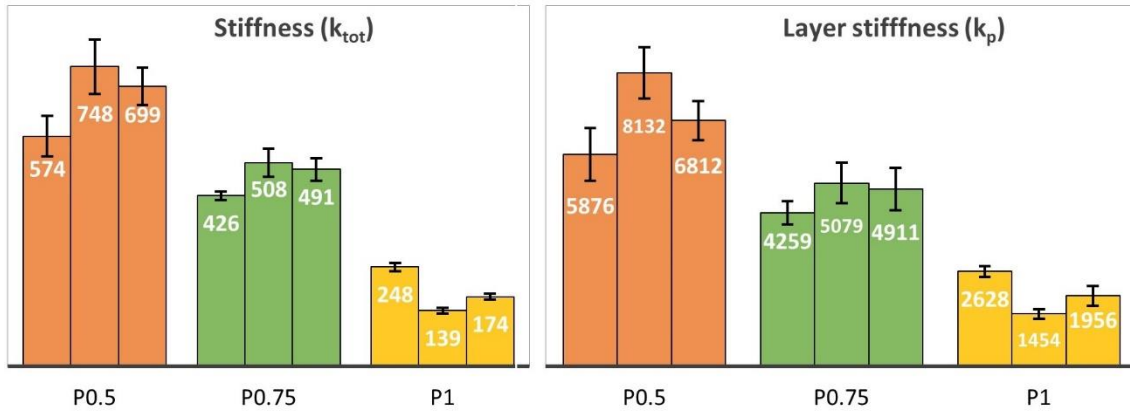| Frame | Load [kN] | ..... | Probe displacement [mm] | | | ..... | $\Delta$displacement [mm] | | ..... | Layer stiffness [kN/mm] | | ..... | $\Delta$tot | $k_{TOT}$ |
|---|---|---|---|---|---|---|---|---|---|---|---|---|---|---|
| | | | 4 | 5 | 6 | | $\Delta$4-5 | $\Delta$5-6 | | $k_{L4}$ | $k_{L5}$ | | | |
| .... | .... | ..... | ..... | ..... | ..... | ..... | ..... | ..... | ..... | ..... | ..... | ..... | ..... | ..... |
| 6 | 16.12 | ..... | 0.031 | 0.027 | 0.022 | ..... | 0.004 | 0.005 | ..... | 4029 | 3223 | ..... | 0.041 | 393 |
| 7 | 19.23 | ..... | 0.035 | 0.031 | 0.025 | ..... | 0.004 | 0.006 | ..... | 4808 | 3205 | ..... | 0.047 | 409 |
| 8 | 22.18 | ..... | 0.043 | 0.037 | 0.031 | ..... | 0.006 | 0.006 | ..... | 3697 | 3205 | ..... | 0.057 | 389 |
| ... | ... | ... | ... | ... | ... | ... | ... | ... | ..... | ..... | ..... | ..... | ..... | ..... |

Figure 6: Structures stiffness: mean values and standard deviations of overall (left) and layer (right) stiffness of periodic lattice structures for all frames.

Table 3: Summary of measured ($k_{TOT}$ and $k_L$) and calculated stiffness ($k_U$).

|  | Mean P0.5 | Std. Dev | Mean P0.75 | Std. Dev | Mean P1 | Std. Dev |
|---|---|---|---|---|---|---|
| Stiffness ($k_{TOT}$) [kN/mm] | 674 | 90 | 396 | 67.3 | 187 | 56 |
| Layer stiffness ($k_L$) [kN/mm] | 6940 | 1134 | 4749 | 433 | 2013 | 589 |
| Unit stiffness ($k_U$) [kN/mm] | **108** | 17.7 | **74** | 6.8 | **31** | 9.2 |

Based on knowledge of the stiffness of the single P1, P0.75 and P0.5 units (Table 3), it was possible to calculate the overall stiffness of any complex and graded structure designed with these elementary units. In this way, the stiffnesses of the FG1 and FG2 structures (Figure 2) were estimated analytically as 392 kN/mm and 321 kN/mm, respectively.

*3.1.2 Stiffness prediction and experimental validation of FG structures*

In order to validate the stiffness prediction of the functionally graded structures, compressive tests and DIC analyses were repeated for the FG1 and FG2 lattice structures (three samples of each type). The test procedure and data processing techniques remained unchanged. Figure 7a shows the displacement maps of the FG1 and FG2 lattice structures. The probe points (from 1 to 10) for displacement measurement of each FG1 layer for the last frame acquired in the elastic region, corresponding to a load of 15.9 kN, are highlighted in the Figure 7b. On the right-hand side of the same figure, the displacement of the structure in a central y-z section is shown. The changing slope of the curve from the P1 layer to the P0.75 and P0.5 layers underlines the different stiffnesses of these layers and the localized nature of displacement in the low-stiffness part. This localization also hides stiffness differences between the P0.75 and P0.5 layers and the solid part.
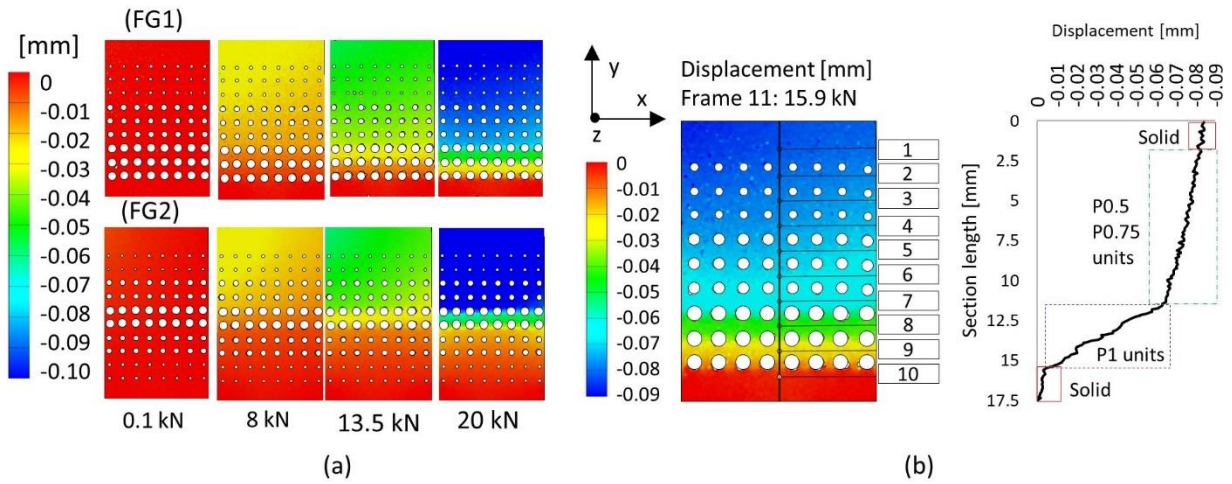
*Figure 7: Displacements: maps of FG1 and FG2 lattice structures (a) and representative curve of FG1.*

Table 4 summarizes the overall stiffness values calculated for the FG1 and FG2 structures, together with comparison of predicted and experimental values. The percentage error was 4.3 % for FG1 and 7.3 % for FG2, thus validating the presented experimental model with good precision.

Table 4: Predicted and measured overall stiffness of FG1 and FG2 structures.

|  | FG1 | FG2 |
|---|---|---|
| Theorical stiffness [kN/mm] | 392 | 321 |
| Experimental stiffness (mean value) [kN/mm] | 409 | 346 |
| Std.Dev. | 68 | 56 |

### 3.2 Stiffness maps

After model validation, a stiffness map for each unit was defined to allow fast design of FG structures with desired compressive stiffness values. Figure 8 shows an array of data representing the overall stiffness of structures built with a number of layers from 1 to 15 (rows) and units per layer from 2x2 to 10x10 (columns) using P0.75 units. The box with the red number highlights the stiffness of the structure used for experiments reported here within (10 layers and 64 units per layer). Similar arrays were also determined for P1 and P0.5.

To further validate the calculated data and stiffness map, samples T0.75 and S0.75 (Figure 3) were subject to the same compressive tests. The predicted stiffnesses of these two samples are shown in Figure 8 within the green and blue boxes, respectively.

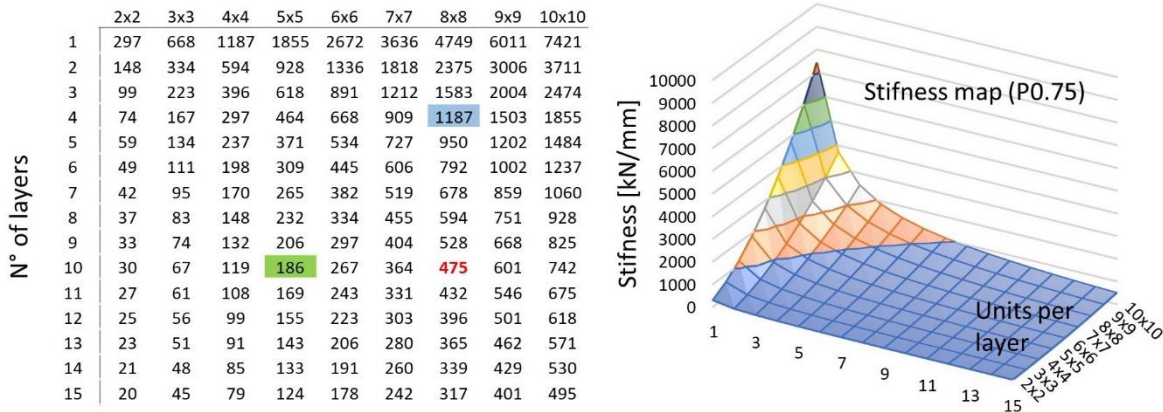| N° of layers | 2x2 | 3x3 | 4x4 | 5x5 | 6x6 | 7x7 | 8x8 | 9x9 | 10x10 |
|---|---|---|---|---|---|---|---|---|---|
| 1 | 297 | 668 | 1187 | 1855 | 2672 | 3636 | 4749 | 6011 | 7421 |
| 2 | 148 | 334 | 594 | 928 | 1336 | 1818 | 2375 | 3006 | 3711 |
| 3 | 99 | 223 | 396 | 618 | 891 | 1212 | 1583 | 2004 | 2474 |
| 4 | 74 | 167 | 297 | 464 | 668 | 909 | 1187 | 1503 | 1855 |
| 5 | 59 | 134 | 237 | 371 | 534 | 727 | 950 | 1202 | 1484 |
| 6 | 49 | 111 | 198 | 309 | 445 | 606 | 792 | 1002 | 1237 |
| 7 | 42 | 95 | 170 | 265 | 382 | 519 | 678 | 859 | 1060 |
| 8 | 37 | 83 | 148 | 232 | 334 | 455 | 594 | 751 | 928 |
| 9 | 33 | 74 | 132 | 206 | 297 | 404 | 528 | 668 | 825 |
| 10 | 30 | 67 | 119 | 186 | 267 | 364 | 475 | 601 | 742 |
| 11 | 27 | 61 | 108 | 169 | 243 | 331 | 432 | 546 | 675 |
| 12 | 25 | 56 | 99 | 155 | 223 | 303 | 396 | 501 | 618 |
| 13 | 23 | 51 | 91 | 143 | 206 | 280 | 365 | 462 | 571 |
| 14 | 21 | 48 | 85 | 133 | 191 | 260 | 339 | 429 | 530 |
| 15 | 20 | 45 | 79 | 124 | 178 | 242 | 317 | 401 | 495 |

Figure 8: Stiffness map: array of values for P0.75 structures with different overall dimensions.

The experiments resulted in average stiffnesses of samples T0.75 and S0.75 equal to 178 kN/mm and 1133 kN/mm, respectively, corresponding to an error of 4.3% and 4.5% in the presented estimation.

### 3.3 Compressive behavior and local/global strain comparison

The compressive load-engineering strain curve of a P1 periodic structure is presented in Figure 9. The graph shows a lattice structure tested up to a compressive strain of 40%, while the main mechanical properties are given in Table 5 as mean values of all tested samples. In the case of P0.5 structures, it was not possible to identify the first relative maximum point (maximum compressive load and strain) due to the maximum load capacity of the cell (100 kN).

Sample failure and highest stress occurred between the holes of horizontally adjacent units (right-hand side of Figure 9).
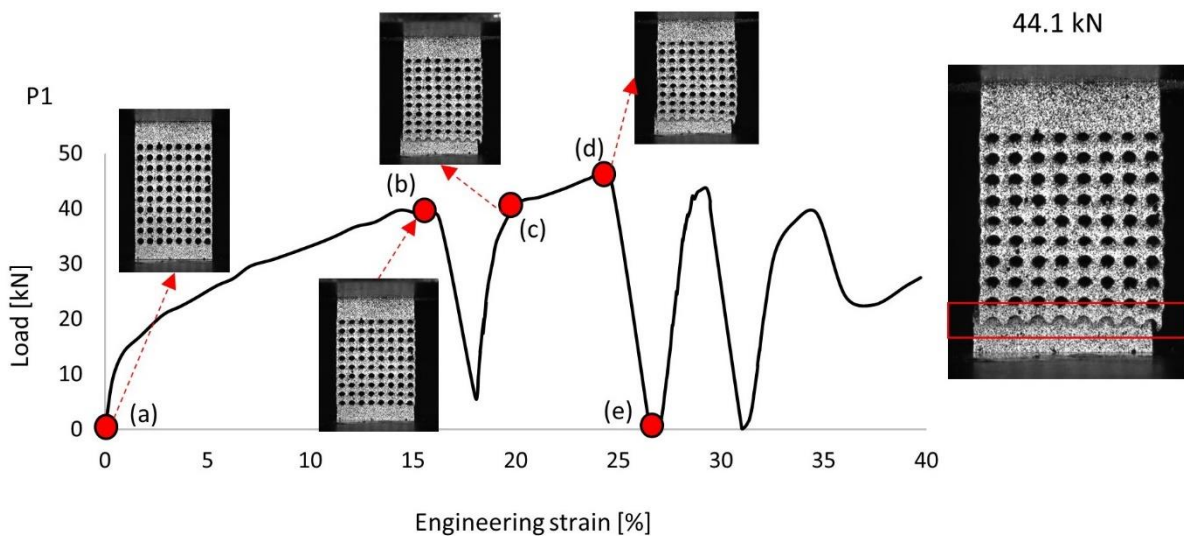


Figure 9: Compressive load-engineering strain curve: behaviour of P1 lattice structure and corresponding frames. The enlargement on the right-hand side shows layer failure at point (d).

For this reason, the cross-sectional area used for stress calculation (Table 5) corresponded to the minimum area, located on a plane perpendicular to the build direction and passing through the center of the unit cells. For more direct comparison of specimen mechanical properties with that of the bulk material, proof and yield strengths were also determined in their equivalent forms by considering a cross-sectional area of 144 mm$^2$ (maximum equivalent area).

Table 5: Mean values and standard deviations (in brackets) of mechanical compressive properties of periodic structures.

| | First maximum compressive load [kN] | Cross sectional area [mm$^2$] | Compressive proof strength [MPa] (ISO 13314:2011 [30]) | Quasi-elastic gradient [ISO 13314:2011] [GPa] | Elongation before failure [%] | Equivalent proof strength [MPa] | Equivalent Yield strength [MPa] |
|---|---|---|---|---|---|---|---|
| P0.5 | / | 50.11 | 1220 (28) | 98 (2.9) | / | 423 (10) | 350 (6.6) |
| P0.75 | 98.6 (2.1) | 34.75 | 1260 (15) | 89 (15.4) | 20.6 (0.6) | 304 (3.6) | 254 (4.9) |
| P1 | 41.3 (0.5) | 15.42 | 1150 (6) | 111 (13.6) | 16.1 (1.1) | 123 (1.4) | 95 (3.2) |

Figure 10 shows the local strain distribution ($\varepsilon_y$ parallel to loading direction) obtained via DIC measurements of the same structure. The enlargement on the right-hand side shows a deformation map identifying three main areas (1-3 in the figure): an elliptical crown (1) that connects two adjacent units with the highest strain (6 % at 21.8 kN), elliptical areas surrounding the crown (2) with average strain (2-4 % at 21.8 kN) and a zone in which strain is almost zero (3), in particular above and below the holes but also in the middle of the ellipse.
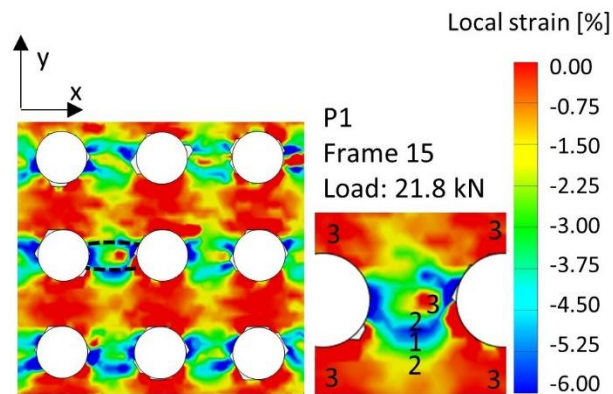


Figure 10: Strain map: local strain in loading direction ($\varepsilon_y$) of P1 structure at the beginning of plastic deformation.

By analyzing the strain maps of all frames, it is possible to identify the beginning of strain localization between 0.4 – 0.6 % engineering strain, becoming evident on all units above 0.8 % engineering strain. This value increases slightly for the P0.75 and P0.5 structures, up to 1.2 % and 1.4 %

respective, while the compressive load-strain behavior and local strain distribution remain unchanged.

The functionally graded structures exhibited the same failure behavior, initially involving the P1 layers as shown in Figure 11a. On the left-hand side of the figure, a frame for the FG1 sample shows the upper layer starting to collapse, while on the right-hand side, the same failure is visible in the middle of the FG2 sample where the P1 layers are located. Figure 11b exhibits a similar load-engineering strain trend for the FG2 structures, as noted previously. For more accurate comparison with periodic structures, the main mechanical properties of the FG lattices are given in Table 6 as mean values across all tested samples.

Table 6: Mean values and standard deviations (in brackets) of mechanical compressive properties of FG structures.

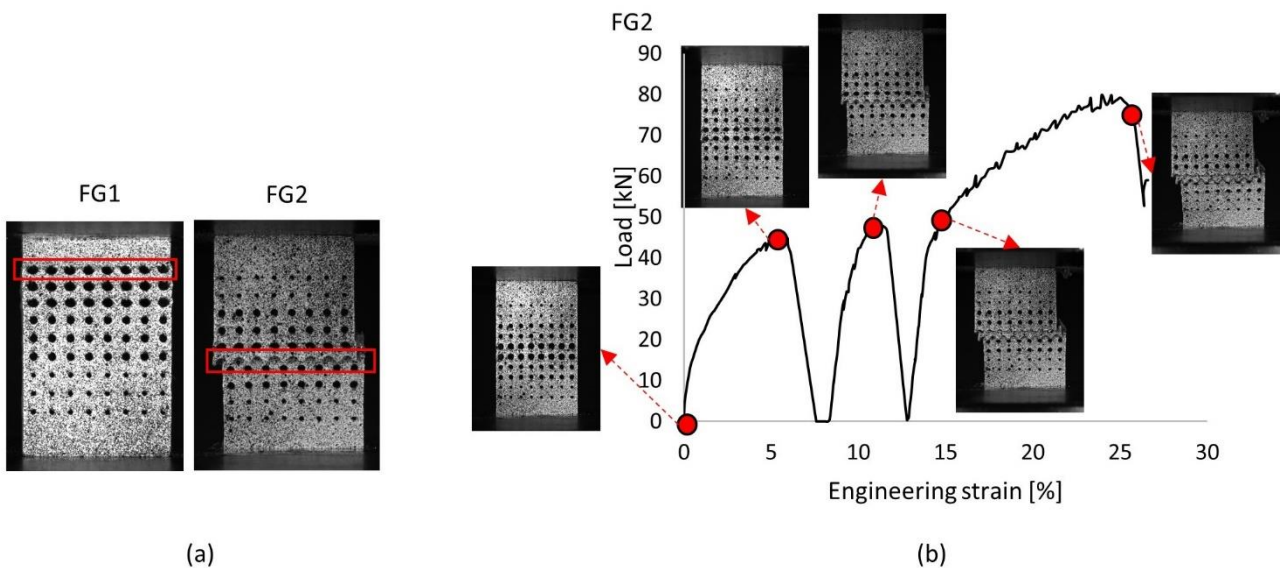|  | First maximum compressive load [kN] | Cross sectional area [mm$^2$] | Compressive proof strength [MPa] (ISO 13314:2011) | Quasi-elastic gradient [ISO 13314:2011] [GPa] | Elongation before failure [%] | Equivalent proof strength [MPa] | Equivalent Yield strength [MPa] |
|---|---|---|---|---|---|---|---|
| FG1 | 44.9 (0.5) | 15.42 | 1525 (65) | 310 (86) | 6.6 (0.1) | 163 (6.9) | 95 (11.7) |
| FG2 | 49.9 (0.7) |  | 1830 (36) | 302 (14) | 5.9 (0.6) | 196 (3.8) | 113 (8.0) |



Figure 11: Compressive load-engineering strain curve: (a) First layer failure of functionally graded structures. (b) Compressive load-engineering strain curves of FG2 and corresponding frames.

Figure 12 shows the overall deformation map of the P1 and FG2 structures, further confirming that both samples have the same local strain distribution, concentrated in the P1 layers in the case of the functionally graded structure.

Robust comparison of the global mechanical behavior of each lattice structure was carried out through analysis of the flow stress curve from the yield point to the first failure. The outcomes of

this analysis are presented in Table 7 in terms of J&C coefficients that were calculated by fitting the J&C model to the flow stress curve of each sample, an example of which is reported in Figure 13. Lattice structure results were also compared with the coefficients obtained for full density samples manufactured by LPBF using the same process parameters [31].
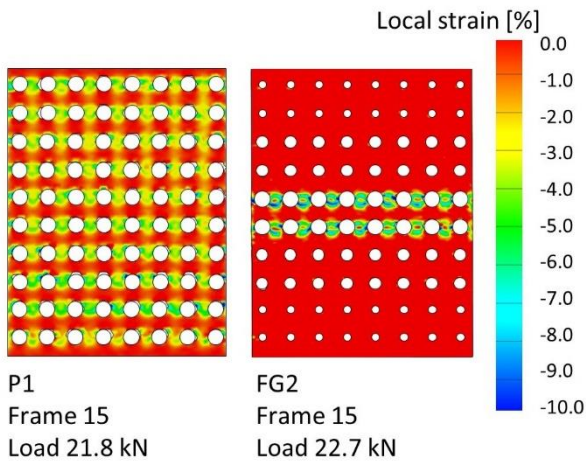


Figure 12: Strain maps: local strains in loading direction (εy) of P1 and FG2 structures.

Table 7: Lattice structure parameters identified using the J&C constitutive model.

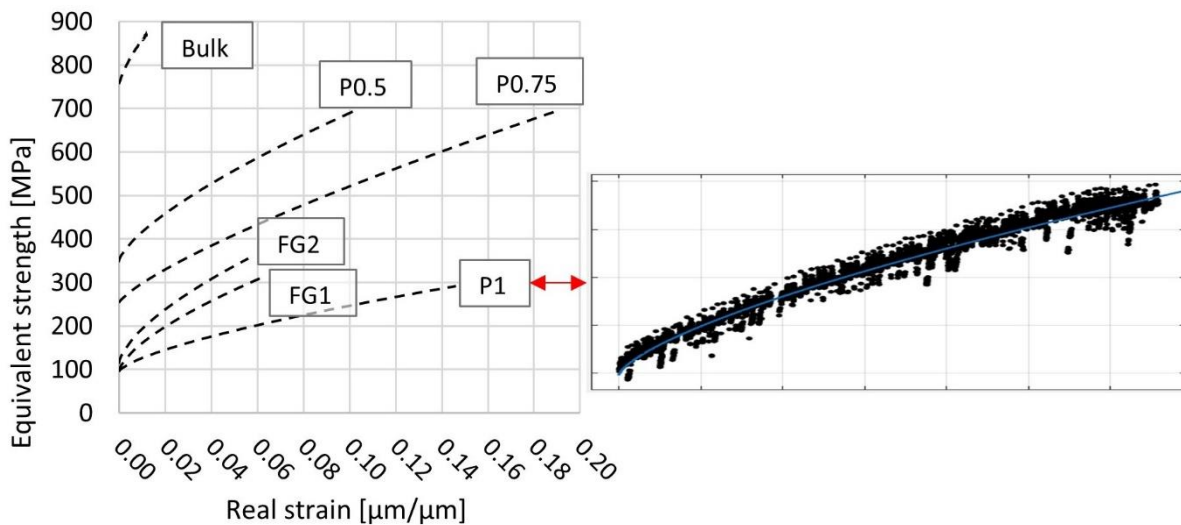|        | A   | Std. Dev | B    | Std. Dev | n     |
|--------|-----|----------|------|----------|-------|
| P0.5   | 350 | 6.65     | 1732 | 115      | 0.708 |
| P0.75  | 254 | 4.85     | 1609 | 22       | 0.779 |
| P1     | 95  | 3.15     | 740  | 25       | 0.688 |
| FG1    | 95  | 11.72    | 1348 | 134      | 0.656 |
| FG2    | 113 | 8.05     | 1545 | 201      | 0.641 |
| Bulk   | 695 | 49       | 2619 | 260      | 0.670 |



Figure 13: Flow stress: periodic and FG lattice structure curves resulting from J&C empirical equation and comparison with full density sample.

### 3.4 Microstructural and geometric defects

Microstructural characterization of samples revealed a typical LPBF microstructure resulting from extremely rapid solidification [32]. A representative low-magnification OM image is reported in Figure 14a. In Figure 14b,c, images obtained with OM using polarized light show epitaxial grain growth crossing over layers. The most evident elongated columnar grains are highlight with two black arrows in Figure 14b. Formation of a keyhole can also be observed in the same figure, recognizable by high depth-to-width ratio of the melt pool. Non-stable keyhole formation causing metal vaporization and gas entrapment, generating porosity at the end of the collapsed melt pool, is visible in Figure 14c. OM analysis shows that this defect takes place in correspondence with the transversal sections close to lower area. These regions are characterized by heat accumulation due to the short time delay between melting of successive layers. Detailed analysis of the specimens highlighted the presence of other defects typical of AM components such as gas porosity and lack of fusion (Figure 14d); however, these were limited and randomly distributed.

In relation to geometric accuracy optical images display complete interconnectivity of the empty areas in all samples (as shows by Fig 14a), however geometric deviations between the nominal and real structures were recognized by deviation between volumes as show in Table 8. Two main errors are responsible for this variation: (i) the upper part of the holes printed in the building direction partially collapsed due to lack of supports, generating an elliptical feature (Figure 14e) and (ii) the real struts size is bigger than the designed one due to the un-melted powder adhesion on the surface.

Table 8: Geometric deviation between real and nominal structures calculated as volumes ratio.

|  | Mean real volume [mm$^3$] | Std. Dev. | Designed volume [mm$^3$] | Deviation [%] |
|---|---|---|---|---|
| P1 | 809 | 13.9 | 794 | 1.84 |
| P0.75 | 1285 | 10.1 | 1219 | 5.11 |
| P0.5 | 1526 | 24.1 | 1448 | 5.15 |
| FG1 | 1081 | 18.1 | 1038 | 3.99 |
| FG2 | 1274 | 8.4 | 1226 | 3.80 |
| S0.75 | 514 | 0.15 | 488 | 5.07 |
| T0.75 | 495 | 3.0 | 476 | 3.75 |

SEM analysis, in fact, revealed that lattice samples presented ~15–100 µm superficial irregularities due to un-melted grains that were sintered to the surface (Figure 14f). These sintered powders were

randomly distributed on the external surface of the lattice and maintained the initial quasi-spherical shape of the metal powder.
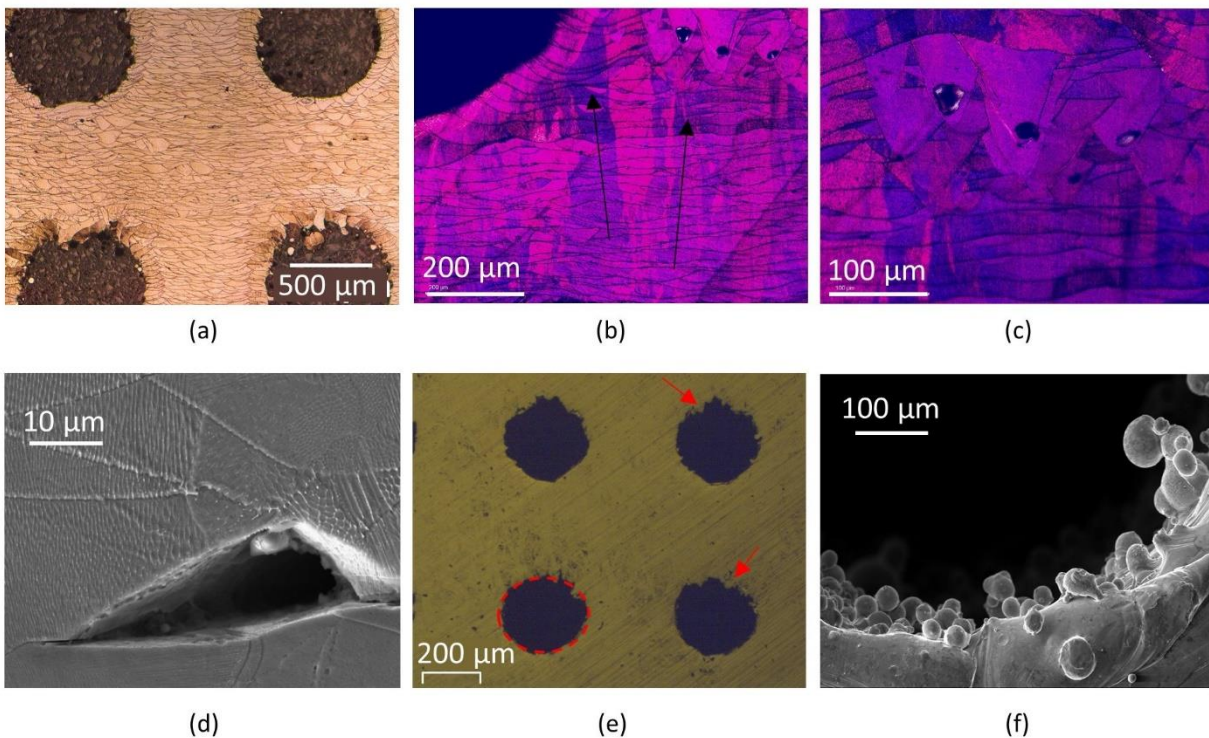


Figure 14: OM and SEM images showing details of the main microstructural and geometric defects of AM lattice structures: (a) gas porosity, (b-c) keyhole porosity, (d) lack of fusion, (d) collapse of unsupported material and (f) sintered powder on sample surface.

## 4. Discussion

Despite there being many studies in the literature dedicated to lattice structures produced by additive manufacturing for various applications, little has been done to define a rigorous method for stiffness prediction of these structures, in particular in the case of FGL structures. The results of the present work should be interpreted in the context of a broader investigation aimed at improving understanding of the mechanical behavior of periodic and FGL structures by ensuring the development of adequate tools to predict such behavior.

A Digital Imaging Correlation technique was chosen to study the compressive behavior of structures to both calculate the stiffness and accurately determine local deformations affecting the analyzed structures. To this end, a preliminary total displacement measurement of all structures in each frame was carried out. The results allowed identification of undesired misalignments between the loaded surfaces, as incorrect positioning of the structures could have potentially compromised the load distribution and deformation response with respect to the build direction and z struts.

Subsequent determination of the displacement of each individual layer required a large quantity of data to be collected to correctly estimate average stiffness values. A brief discussion on this aspect is necessary. In relation to data obtained for P0.75 (Table 2), all layer stiffness values within the elastic range should be equal since the sample comprises a periodic structure with repeated unit cells. It can be noted from Table 2 that this is in fact not the case. The reason for this deviation is partly due to probe positioning, as a small error in the y coordinate of the probe can easily change the displacement measurement by a few microns, distributing the displacement between layers in an inhomogeneous manner. Secondly, as-built structures are inherently anisotropic due to the thermal cycle imposed by LPBF, as highlight by the OM images in Figure 14b,c, and the presence of randomly distributed defects (Figure 14c,d) [33,34]. Accordingly, the procedure was repeated for each frame and layer, making it possible to calculate a reliable average stiffness value. This outcome was confirmed by the low percentage error in FG1 and FG2 stiffness prediction, equal to 4.3 % and 7.3 %, respectively (Table 4). However, validation with a single macroscopic geometry (10 layers and 64 units per layer) was not considered sufficient to evaluate the robustness of the predictive method. For this reason, a stiffness map was defined for each unit (0.5, 0.75 and 1), varying the number of layers (1-15) and units contained within each layer (4-100). Two of these geometries were tested using the same methodology to confirm its reliability. The forecast error in the latter case, however, exhibited comparable values (4.3 – 4.5 %).

A further consideration can be made in relation to the geometric defects revealed by OM and SEM analysis (Figure 14e,f). Unlike microstructural defects such as porosity or lack of fusion, which are randomly distributed, or the effects of anisotropy, which can be reduced or avoided with subsequent heat treatments, geometric defects are repeatable within the units and can only be eliminated with finishing operations, which are complex to manage for such small structures.

As concern the geometric accuracy, the results shown in Table 8 exhibit that the measured volume of the LPBF samples exceed the nominal value in a range between 1.8 % and 5.2 %. The higher experimental volume is attributed to the un-melted powder adhesion on the surface of the lattice due to the high temperature which are maintained in these areas throughout the process and which promote the sintering of the particles. Similar results were obtained by other authors, both on solid and in lattices additively manufactured samples [20,25-26]. However, Yang et al [26] and Choy et al [25] have highlighted an increasing in volume deviation at the ratio of surface area to volume increases, while in this study higher deviations were detected in P0.75 and P0.5 samples where the holes' diameter and surface to volume ratio are lower. This is attributable to the heat cycle involved

during the manufacturing: low-volume structures (e.g. P1), despite being penalized in terms of thermal conductivity with the build platform, requires shorter laser-powder interaction times and consequently are subjected at less overheating which promote the adhesion of the surrounding powders on the surface.

Moreover, the geometric accuracy decreased by overhanging surfaces and in particular the upper part of the circular holes, resulting in rougher and geometrically distorted surfaces that take on an elliptical shape. These holes' deformation is one of the causes that makes complex the prediction of the mechanical behavior of lattice structures. An interesting development would be the comparison of experimental values with simulation results conducted with finite element software (FEM model) to discriminate the effects of the real geometry compared to the nominal structure.

In relation to mechanical behavior, all lattice structures exhibited the same compressive behavior. Figures 9 and 11 show steep linear increases in the load-strain curve without a plateau (points a → b in Fig. 9) up to the first relative maximum value (point b). Beyond point b, collapse of the first layer occurs with a consequent decrease in load. As the adjacent layers come back into contact, the load increases again, exceeding the maximum force obtained at point b due to compaction of the structure (points c → d). This load increase continues until the next layer fails (point e) and so forth until the lattice collapses. This type of mechanical behavior is defined in the literature as stretch dominant deformation [35], in which plastic deformation of the structure is mainly controlled by the z struts. Therefore, these struts act as reinforcement of the entire lattice and are subject to the highest localized deformation.

For this type of unit, plastic deformation begins with the formation of a "high stress plane" with localized deformation, oriented perpendicular to the applied stress. Focusing on the layers of interest, a deformation map can be obtained (Figure 10). Maximum deformation was distributed within an ellipse connecting adjacent units. This strain localization was probably caused by local variations in the cross-sectional area of the z struts within these unit designs, amplified by process-related defects around these fine features. For instance, with reference to Figures 9 and 10 for a nominal compression strain of 3.4 % at 21.8 kN, local strains measured by DIC were 6 %, which is approximately 176 % of the global value, in line with other studies [36].

Finally, detailed analysis of global mechanical behavior was carried out. By observing Tables 5 and 6 and Figures 10 and 11, it is interesting to note that functionally graded structures exhibited less ductile mechanical behavior, with elongation before fracture 60% lower than P1 samples and proof

strength 33% and 59% higher than FG1 and FG2 samples, respectively. Flow stress data and determination of J&C coefficients also highlighted greater hardening of the periodic structures compared to the FG ones. The same values could be used for FEM simulations in future works, as previously proposed by other authors [37].

## 5. Conclusion

In the present work, stiffness prediction and deformation analysis of Cobalt-Chromium lattice structures manufactured using an LPBF additive process were carried out. The study was developed in two steps, the first comprising initial compressive tests and DIC analysis performed on periodic structures, the second exploiting these results to predict the stiffness of two types of functionally graded structures. The proposed method was validated through comparison with experimental results, thus allowing accurate estimation of the stiffness of complex structures designed with the proposed elementary units. The mechanical properties and deformation behavior of these structures were also investigated, with the local strain distribution mapped and compared with global deformation values.

The following conclusions can be drawn from the obtained results.

1) DIC analysis on lattice structures allows the elastic stiffness of each layer to be measured and the single unit stiffness to be calculated. The units studied in this work exhibited stiffness values in the range 108-31 kN/mm. Prediction of the overall stiffness of FG structures with this method led to an error of less than 7.3 % for structures of the same macroscopic size and less than 4.5 % for periodic structures of different macroscopic size.

2) The proposed stiffness prediction method can be applied to any material and elementary unit. However, in the design of the FG structures, the model is effective for lattices obtained by replicating units with discrete porosity. Furthermore, the DIC acquisition system must be chosen on the basis of the proposed unit and may require a multi-camera system n case of high-complex geometries.

3) Load-strain behavior exhibited a stretch dominant failure mode, with a strain distribution map defined and confirmed for all tested structures. By comparing the global and local strain for the same frame, the global strain assumed values as much as 56 % lower than the maximum localized value.

4) Johnson and Cook coefficients were identified for periodic and FG structures and were subsequently compared to values obtained for full density samples produced with LPBF using the same process parameters. These coefficients can be used in numerical simulations.

5) Future works must now focus on finite element simulations and/or analytical calculations to correlate experimental and modeled stiffness data, thus allowing the impact of manufacturing errors such as microstructural and geometric defects or anisotropy to be defined. Identification of the main mechanical properties of lattice structures, corrected with appropriate coefficients that consider manufacturing defects, would make it possible to quickly estimate the behavior of complex lattice structures integrated into real components. These lattice structures can be modeled as full density components to reduce the computational load by employing equivalent mechanical properties based on measured values.

## Acknowledgements

## Reference

[1] Lou S, Pagani L, Zeng W, Jiang X, Scott PJ. Watershed Segmentation of Topographical Features on Freeform Surfaces and Its Application to Additively Manufactured Surfaces. Precis Eng 2020; 63: 177-186. doi: 10.1016/j.precisioneng.2020.02.005

[2] Maconachie T, Leary M, Lozanovski B, Zhang X, Qian M, Faruque O, Brandt M. SLM lattice structures: Properties, performance, applications and challenges, Mater Des 2019; 183: 108137. doi: 10.1016/j.matdes.2019.108137

[3] Wang Y, Zhang L, Daynes S, Zhang H, Feih S, Wang MY. Design of graded lattice structure with optimized mesostructures for additive manufacturing. Mater Des 2018; 142: 114-123. doi: 10.1016/j.matdes.2018.01.011

[4] Liu PS, Ma XM. Property relations based on the octahedral structure model with body-centered cubic mode for porous metal foams. Mater Des 2020; 188: 108413. doi: 10.1016/j.matdes.2019.108413

[5] Zadpoor AA. Mechanical performance of additively manufactured meta-biomaterials. Acta Biomater 2019; 85: 41-59. doi: 10.1016/j.actbio.2018.12.038

[6] Dong G, Tang Y, Zhao FY. A survey of modeling of lattice structures fabricated by additive manufacturing. J Mech Des 2017; 139(10): 100906-13. doi: 10.1115/1.4037305

[7] Yu S, Sun J, Bai J. Investigation of functionally graded TPMS structures fabricated by additive manufacturing. Mater Des 2019; 182: 108021. doi: 10.1016/j.matdes.2019.108021

[8] Al-Ketan O, Rowshan R, Abu Al-Rub RK. Topology-mechanical property relationship of 3D printed strut, skeletal, and sheet based periodic metallic cellular materials. Addit Manuf 2018; 19: 167-183. doi: 10.1016/j.addma.2017.12.006

[9] Dressler AD, Jost EW, Miers JC, Moore DG, Seepersad CC, Boyce BL. Heterogeneities dominate mechanical performance of additively manufactured metal lattice struts. Addit Manuf 2018; 28: 692-703. doi: 10.1016/j.addma.2019.06.011

[10] Bhate D, Penick CA, Ferry LA, Lee C. Classification and Selection of Cellular Materials in Mechanical Design: Engineering and Biomimetic Approaches. Designs 2019; 3(1): 19. doi: 10.3390/designs3010019

[11] Syam WP, Jianwei W, Zhao B, Maskery I, Elmadih W, Leach R. Design and analysis of strut-based lattice structures for vibration isolation. Precis Eng 2018; 52: 494-506. doi: 10.1016/j.precisioneng.2017.09.010

[12] Catchpole-Smith S, Sélo RRJ, Ashcroft IA, Tuck CJ, Clare A, Davis AW. Thermal conductivity of TPMS lattice structures manufactured via laser powder bed fusion. Addit Manuf 2019; 30: 100846. doi: 10.1016/j.addma.2019.100846

[13] Nagesha BK, Chalawadi D, Dhinakaran V, Varsha Shree M, Manoj Kumar KP, Sathish T. Review on characterization and impacts of the lattice structure in additive manufacturing. Mater Today: Proc 2020; 21: 916-919. doi: 10.1016/j.matpr.2019.08.158

[14] Caravaggi P, Liverani E, Leardini A, Fortunato A, Belvedere C, Baruffaldi F, Fini M, Parrilli A, Mattioli-Belmonte M, Tomesani L, Pagani S. CoCr porous scaffolds manufactured via selective laser melting in orthopedics: Topographical, mechanical, and biological characterization. J Biomed Mater Part B 2019; 107(7):2343-2353. doi: 10.1002/jbm.b.34328.

[15] Pagani S, Liverani E, Giavaresi G, De Luca A, Belvedere C, Fortunato A, Leardini A, Fini M, Tomesani L, Caravaggi P. Mechanical and in vitro biological properties of uniform and graded cobalt-chrome lattice structures in orthopedic implants. J Biomed Mater Part B, *under review*

[16] Carluccio D, Xu C, Venezuela J, Cao Y, Kent D, Bermingham M, Ali Gokhan D, Previtali B, Qingsong Y, Dargusch M. Additively manufactured iron-manganese for biodegradable porous load-bearing bone scaffold applications. Acta Biomater 2020; 103: 346-360. doi: 10.1016/j.actbio.2019.12.018

[17] Yan X, Li Q, Yin S, Chen Z, Jenkins R, Chen C, Wang J, Ma W, Bolot R, Lupoi R, Ren Z, Liao H, Liu M. Mechanical and in vitro study of an isotropic Ti6Al4V lattice structure fabricated using selective laser melting. J Alloys Compd 2019; 782: 209-22. doi: 10.1016/j.jallcom.2018.12.220

[18] Zhou H, Zhao H, Ma Z, Zhang DZ, Fu G. Sheet and network based functionally graded lattice structures manufactured by selective laser melting: Design, mechanical properties, and simulation. Int J Mech Sci 2020; 175: 105480. doi: 10.1016/j.ijmecsci.2020.105480

[19] Panesar A, Abdi M, Hickman D, Ashcroft I. Strategies for functionally graded lattice structures derived using topology optimisation for Additive Manufacturing. Addit Manuf 2018; 19: 81-94. doi: 10.1016/j.addma.2017.11.008

[20] Wang S, Liu L, Li K, Zhu L, Chen J, Hao Y. Pore functionally graded Ti6Al4V scaffolds for bone tissue engineering application. Mater Des 2019; 168: 107643. doi: 10.1016/j.matdes.2019.107643

[21] Zargarian A, Esfahanian M, Kadkhodapour J, Ziaei-Rad S, Zamani D. On the fatigue behavior of additive manufactured lattice structures. Theor Appl Fract Mech 2019; 100: 225-232. doi: 10.1016/j.tafmec.2019.01.012

[22] Ravari MK, Esfahani SN, Andani MT, Kadkhodaei M, Ghaei A, Karaca H, Elahinia M. On the effects of geometry, defects, and material asymmetry on the mechanical response of shape memory alloy cellular lattice structures, Smart Mater Struct 2016; 25(2). doi: 10.1088/0964-1726/25/2/025008

[23] Lozanovski B, Leary M, Tran P, Shidid D, Qian M, Choong P, Brandt M. Computational modelling of strut defects in SLM manufactured lattice structures. Mater Des 2019; 171: 107671. doi: 10.1016/j.matdes.2019.107671

[24] Choy S Y, Sun C, Leong K F, Wei J. Compressive properties of functionally graded lattice structures manufactured by selective laser melting. Mater Des 2017; 131: 112-120. doi: 10.1016/j.matdes.2017.06.006

[25] Choy S Y, Sun C, Sin W J, Leong K F, Su P. Superior energy absorption of continuously graded microlattices by electron beam additive. Virtual Phys Prototy 2021; 16: 14-28. doi: 10.1080/17452759.2020.1868656

[26] Yang L, Han C, Wu H, Hao L, Wei O, Yan C, Shi Y. Insights into unit cell size effect on mechanical responses and energy absorption capability of titanium graded porous structures manufactured by laser powder bed fusion. J Mech Behav Biomed Mater 2020; 109: 103843. doi: 10.1016/j.jmbbm.2020.103843

[27] Sudarmadji N, Tan J Y, Leong K F, Chua C K, Loh Y T. Investigation of the mechanical properties and porosity relationships in selective laser-sintered polyhedral for functionally graded scaffolds. Acta Biomater 2011; 7(2): 530–537 doi: 10.1016/j.actbio.2010.09.024

[28] Goriainov V, Cook R, Latham JM, Dunlop DG, Oreffo RO. Bone and metal: An orthopaedic perspective on osseointegration of metals. Acta Biomater 2014; 10: 4043–4057 doi: 10.1016/j.actbio.2014.06.004.

[29] Majzoobi GH, Rahimi Dehgolan F. Determination of the constants of damage models. Proc Eng 2011; 10: 764-773. doi: 10.1016/j.proeng.2011.04.127

[30] ISO 13314: 2011. Mechanical testing of metals - Ductility testing - Compression test for porous and cellular metals. https://www.iso.org/standard/53669.html (2011).

[31] Liverani E, Fortunato A, Leardini A, Belvedere C, Siegler S, Ceschini L, Ascari A. Fabrication of Co–Cr–Mo endoprosthetic ankle devices by means of Selective Laser Melting (SLM). Mater Des 2016; 106: 60-68. doi: 10.1016/j.matdes.2016.05.083

[32] Liverani E, Toschi S, Ceschini L, Fortunato A. Effect of selective laser melting (SLM) process parameters on microstructure and mechanical properties of 316L austenitic stainless steel. J Mater Proces Tech 2017; 249: 255-263. doi: 10.1016/j.jmatprotec.2017.05.042

[33] Charmi A, Falkenberg R, Ávila L, Mohr G, Sommer K, Ulbricht A, Sprengel M, Saliwan Neumann R, Skrotzki B, Evans A. Mechanical anisotropy of additively manufactured stainless steel 316L: An experimental and numerical study. Materi Sci Eng A 2021; 799: 140154. doi: 10.1016/j.msea.2020.140154

[34] Liu L, Kamm P, García-Moreno F, Banhart J, Pasini D. Elastic and failure response of imperfect three-dimensional metallic lattices: the role of geometric defects induced by Selective Laser Melting. J Mech Phys Solids 2017; 107: 160-184. doi: 10.1016/j.jmps.2017.07.003.

[35] Hanks B, Berthel J, Frecker M, Simpson TW. Mechanical properties of additively manufactured metal lattice structures: Data review and design interface. Addit Manuf 2020; 35: 101301. doi: 10.1016/j.addma.2020.101301

[36] Köhnen P, Haase C, Bültmann J, Ziegler S, Schleifenbaum JH, Bleck W. Mechanical properties and deformation behavior of additively manufactured lattice structures of stainless steel. Mater Des 2018; 145: 205-217. doi: 10.1016/j.matdes.2018.02.062

[37] Zhou H, Zhao M, Ma Z, Zhang D Z, Fu G. Sheet and network based functionally graded lattice structures manufactured by selective laser melting: Design, mechanical properties, and simulation. Int. J. Mech. Sci. 2020; 175: 105480. doi: 10.1016/j.ijmecsci.2020.105480